

Structure and magnetism of the $\text{Ba}_6\text{Y}_2\text{Rh}_2\text{Ti}_2\text{O}_{17}$ hexagonal perovskite

Loi T. Nguyen, Daniel B. Straus and R. J. Cava

Department of Chemistry, Princeton University, Princeton, New Jersey 08544, USA

ABSTRACT

We report the synthesis and initial characterization of $\text{Ba}_6\text{Y}_2\text{Rh}_2\text{Ti}_2\text{O}_{17}$, a hexagonal perovskite, prepared at ambient pressure in air at 1500°C . In the crystal structure, face-sharing RhO_6 octahedra form Rh_2O_9 dimers in a layered triangular geometry. The material displays a small effective magnetic moment, which must arise from the Rh ions present, and a negative Curie-Weiss temperature. The transport band gap and optical band gaps are very similar, near 0.16 eV, and thus $\text{Ba}_6\text{Y}_2\text{Rh}_2\text{Ti}_2\text{O}_{17}$ is a semiconductor. A large upturn in the heat capacity at temperatures below 1 K, suppressed by magnetic fields larger than 2 Tesla, is observed. A very large Sommerfeld-like T-linear term in the specific heat ($\gamma=166$ mJ/mol f.u- K^2) is seen, although the material is highly insulating at low temperatures. These results suggest the possibility of a spin liquid ground state in this material.

Keywords: hexagonal perovskite, face-sharing octahedra, magnetic rhodium oxide, spin liquid.

INTRODUCTION

After the discovery of superconductivity in $\text{Na}_{0.35}\text{CoO}_2 \cdot 1.6\text{H}_2\text{O}$ ^{1,2}, the search for structurally and chemically related superconductors became of significant interest³⁻⁵. A metal-insulator transition was found in Na_xRhO_2 at $x = 0.67$, for example, but superconductivity was not observed³. This was attributed by some researchers to the strong spin-orbit coupling present for the $4d$ transition metal Rh, which defeats the superconductivity^{3,4,6,7}. Rhodium-based compounds exhibit a variety of other interesting properties, however, from photocatalyst and photo-electrolytic electrodes (e.g. LuRhO_3 ⁸ and AgRhO_2 ⁹) to intermetallic superconductors, $\text{Y}_2\text{Rh}_3\text{Si}_5$ ($T_c=4.4$ K)¹⁰, Zr_2Rh ($T_c=11.2$ K)¹¹, TaRh_2B_2 ($T_c=5.8$ K) and NbRh_2B_2 ($T_c=7.6$ K)¹².

Spin liquids display a novel magnetic state in which the magnetic moments remain fluctuating down to temperatures near absolute zero. In quantum spin liquids (QSLs) the magnetic wave functions are entangled at low temperatures. Although at the time of this writing no QSL material is universally accepted, candidates are frequently members of the magnetically frustrated family of materials, because in such cases there is a degeneracy of equivalent energy states present at low temperatures. Although there appears to be no single experimental characteristic that signifies the presence of a QSL state, candidates often show the absence of conventional magnetic ordering, a broad continuum of magnetic excitations in inelastic neutron scattering spectra, and large upturns in the heat capacity at low temperatures. QSL candidates have been proposed based on copper, cobalt, ruthenium, iridium, and rare earth ions¹³⁻²⁴.

Here we report a new kind of candidate material, a rhodium-oxide-based compound that shows some of the characteristics of a spin liquid. This rhodate, $\text{Ba}_6\text{Y}_2\text{Rh}_2\text{Ti}_2\text{O}_{17}$, synthesized in air at ambient pressure at 1500°C , is an ordered hexagonal perovskite analogous to $\text{Ba}_6\text{Y}_2\text{Ti}_4\text{O}_{17}$ ²⁵. The crystal structure is based on Rh_2O_9 dimers, made from two face-sharing RhO_6 octahedra, in a

layered triangular array. The distance between two Rh ions within the dimer is about 2.6 Å, allowing for strong Rh-Rh interactions. The triangular layers of dimers are well-separated by non-magnetic YO₆ octahedra and TiO₄ tetrahedra. Hence, there may be competition between the magnetic interactions within the Rh₂O₉ dimers and the in-plane and out of plane magnetic interactions in the three-dimensional structure made from stacked triangular layers of dimers. The material is a semiconductor with transport and optical band gaps of about 0.16 eV, effective magnetic moment of about 1.5 μB per formula unit, a Curie Weiss theta of about -2.8 K, no magnetic ordering observed down to 0.35 K, and an anomalous heat capacity is seen at low temperatures. The magnetic moment, which is low but present, makes this a rare but not unique example of a magnetic rhodium oxide^{4,16,26,27}. The heat capacity at low temperatures (~0.35 K) follows a power law with an exponent of 0.57, much smaller than the expected value of 3, and shows an upturn under zero applied magnetic field that is suppressed by applied fields larger than 2 Tesla. Only about 1/3 of the magnetic entropy expected for a spin ½ system is recovered on heating from very low temperatures in zero field, suggesting that spin fluctuations hold on to a significant amount of magnetic entropy at very low temperatures in this material. Finally, the presence of heavy quasiparticles in this electrically insulating spin liquid candidate is supported by the large observed Sommerfeld constant, 166 mJ/mol f.u-K².^{17,23,28}

EXPERIMENTAL

A polycrystalline sample of Ba₆Y₂Rh₂Ti₂O₁₇ was synthesized by solid-state reaction using BaCO₃ (dried in the oven at 120°C for 3 days), Y₂O₃ (dried in the furnace at 1000°C overnight), RhO₂ and TiO₂ (Alfa Aesar, 99.9%, 99.99%, 99.9%, and 99.9%, respectively) in stoichiometric ratios as starting materials. The reagents were mixed thoroughly, placed in alumina crucibles, and heated in air at 900 °C for 24 hours. The resulting powder was reground, pressed into pellets, and

heated in air at 1100, 1300 and 1500°C for 24 hours at each temperature. The phase purity and crystal structure were determined through powder X-ray diffraction (PXRD) using a Bruker D8 Advance Eco with Cu K α radiation and a LynxEye-XE detector. The structure refinement was performed with GSAS²⁹. The crystal structure drawings were created by using the program VESTA³⁰.

The SEM/EDS characterization was performed by using a XL30 FEG-SEM equipped with an EVEX EDS in-situ Tensile Stage, and a Gatan MiniCL imaging system. This high-resolution field-emission SEM has an optimum image resolution of 2nm. The EDS system provides X-ray acquisition characteristics sufficient for obtaining a high-resolution two-dimensional elemental distribution map over the sample surface.

The magnetic susceptibility of Ba₆Y₂Rh₂Ti₂O₁₇ powder was measured in a Quantum Design Physical Property Measurement System (PPMS) DynaCool equipped with a VSM option. The magnetic susceptibilities between 1.8 and 300 K, defined as M/H, where M is the sample magnetization and H is the applied field, were measured at different applied magnetic fields. The sample was pressed, sintered, and cut into pieces with the approximate size 1.0 × 2.0 × 1.0 mm³. for the transport measurement. The resistivity was measured by the dc four-contact method in the temperature range 200 to 300 K in the PPMS. Four Pt contact wires were connected to the samples using silver paint. Below 200 K the sample resistance was too high to be accurately characterized. The specific heat was measured from 200 to 1.8 K in the PPMS DynaCool equipped with a heat capacity option, and to temperatures down to 0.35 K by using a ³He system in the PPMS.

The optical bandgap was determined by using a Thermo Scientific Nicolet 6700 FT-IR spectrometer with an ATR sample holder. The bandgap was estimated from the observed absorption data based on the relation $\alpha h\nu = A(h\nu - E_g)^n$, where A is a constant, α is the absorption

coefficient (cm^{-1}), E_g is the bandgap, and n is 0.5 for a direct transition ($n = 2$ for an indirect transition).

Thermogravimetric Analysis (TGA) was conducted using a TA Instruments SDT Q600 under flowing Ar:H₂ (95:5%). Around 10 mg of Ba₆Y₂Rh₂Ti₂O₁₇ was loaded into an alumina pan and heated from 25°C to 1000°C at the rate 0.5°C/hr. The sample was kept at 1000°C for 30 min, then cooled to room temperature at the rate 5°C/hr. The phase assemblage of the final mixture was determined by using powder XRD.

RESULTS and DISCUSSION

Ba₆Y₂Rh₂Ti₂O₁₇ crystallizes in a hexagonal structure with the space group $P6_3/mmc$ (No. 194). Its powder X-ray diffraction pattern and structural refinement are shown in **Figure 1**. The structure of Ba₆Y₂Ti₄O₁₇ was employed as a starting model for the refinement²⁵ - in the current case the Ti occupies only the layers of tetrahedra while only the Rh are found in the dimers. The structural refinement is of excellent quality and indicated the absence of Ti/Rh/Y mixing disorder to within the sensitivity of the method (a few percent). The inset to **Figure 1** shows the SEM and EDS images collected on the powder sample to confirm that all the elements are present in a single substance. While a variety of Rh⁴⁺ compounds have been synthesized under high pressure, such as BaRhO₃, CaRhO₃, SrRu_{1-x}Rh_xO₃, Sr₄Rh₃O₁₀, and Lu₂Rh₂O₇^{8,27,31-35}, to our knowledge, Ba₆Y₂Rh₂Ti₂O₁₇ appears to be the only Rh₂O₉ dimer compound synthesized at ambient pressure.

Figure 1b shows the TGA data of Ba₆Y₂Rh₂Ti₂O_{17- δ} , reduced under the flow of Ar:H₂ (95:5%) from 25 to 1000°C. The final product is a mixture of Rh, BaTiO₃ and Ba₄Y₂O₇, identified by using power XRD. The mass loss is calculated to be around 3.5%, implying that the empirical formula may be oxygen deficient, at Ba₆Y₂Rh₂Ti₂O_{17- δ} ($\delta \approx 0.5$).

The crystal structure of $\text{Ba}_6\text{Y}_2\text{Rh}_2\text{Ti}_2\text{O}_{17}$ is shown in **Figure 2a**, where two RhO_6 octahedra are face-sharing to form a Rh_2O_9 dimer. In one unit cell, there are two Rh_2O_9 dimers linked by YO_6 octahedra and TiO_4 tetrahedra. The Rh^{4+} -based dimers are arranged in a triangular lattice as shown in **Figure 2b**. The distance between two Rh atoms within a dimer is quite short (2.60 Å) indicating strong chemical interactions between them or even a metal-metal bond. This short Rh-Rh bond length has previously been seen in $\text{Sr}_5\text{Rh}_4\text{O}_{12}$ ³⁶, which displays Rh–O chains in its crystal structure. There are two kinds of Rh-O bond lengths in the Rh_2O_9 dimer in $\text{Ba}_6\text{Y}_2\text{Rh}_2\text{Ti}_2\text{O}_{17}$: 2.21 Å to the outer oxygens, and 2.16 Å to the oxygens between the Rh ions, consistent with the presence of strong Rh-Rh interactions, which shorten the Rh-O bonds. Thus there are likely three types of dominant magnetic interactions in $\text{Ba}_6\text{Y}_2\text{Rh}_2\text{Ti}_2\text{O}_{17}$, dimer-dimer in-plane interactions ($d = 5.92$ Å), plane to plane interactions of the dimers ($d=14.75$ Å, and interactions within the dimers ($d = 2.60$ Å)-as shown in **Figures 2a-c**. The structural parameters determined in the refinement are summarized in **Table 1** and selected bond lengths are listed in **Table 2**.

The temperature-dependent magnetic susceptibility of $\text{Ba}_6\text{Y}_2\text{Rh}_2\text{Ti}_2\text{O}_{17}$ measured under the applied magnetic field of 2 kOe is shown in **Figure 3**. By applied fields of 5 T, however (data not shown) the low temperature susceptibility appears to be lower by a factor of 2. This is due to curvature in the M vs H behavior in high fields and the definition of susceptibility as $\Delta M/\Delta H$ and does not represent the intrinsic low field susceptibility of this substance. The inset in **Figure 3** shows the magnetization as a function of applied magnetic field from 0-9 T at different temperatures. The M vs. H curves are linear above 10 K, and become curved below 10 K, which agrees well with the deviation observed in the temperature-dependent magnetic susceptibility measured in fields of 2 T and higher. There is no sign of magnetic saturation up to 9 T at temperatures down to 1.8 K.

Figure 4 shows the magnetic susceptibility of $\text{Ba}_6\text{Y}_2\text{Rh}_2\text{Ti}_2\text{O}_{17}$ from 1.8-300 K in a 2 kOe applied magnetic field. Above 200 K, the magnetic susceptibility almost reaches zero. Curie-Weiss fitting from 10-50 K results in the Curie-Weiss temperature of -2.8 K and an effective moment of $0.76 \mu_{\text{B}}/\text{mol-Rh}$ as seen in the inset of **Figure 4**. The small negative Curie-Weiss temperature implies the dominance of weak anti-ferromagnetic interactions and the relatively low moment observed compared to that expected in an ionic picture for isolated Rh^{4+} spin $\frac{1}{2}$ ions ($1.73 \mu_{\text{B}}$) will be of interest in the theoretical treatment of this material.

In comparison, in $\text{Ba}_9\text{Rh}_8\text{O}_{24}$, the fact that the magnetic susceptibility does not follow the Curie-Weiss law has been attributed to the presence of non-magnetic Rh^{3+} ions that interrupt the exchange interactions between Rh^{4+} ions, resulting the disruption in magnetic interactions within a chain³⁷. In the rhodate family, Sr_4RhO_6 known to be the first magnetically ordered Rh^{4+} compound has the antiferromagnetic transition temperature at 7 K and the effective moment of $1.71 \mu_{\text{B}}/\text{mol-Rh}$, as expected for moment of spin $\frac{1}{2}$. Although both $\text{Ba}_6\text{Y}_2\text{Rh}_2\text{Ti}_2\text{O}_{17}$ and Sr_4RhO_6 compounds have Rh^{4+} oxidation state ($S = \frac{1}{2}$), $\text{Ba}_6\text{Y}_2\text{Rh}_2\text{Ti}_2\text{O}_{17}$ has much smaller Curie-Weiss temperature and effective moment, this implies a delocalization of the moment among the Rh and O in the dimers.

The inset in **Figure 4** shows the FC/ZFC dc susceptibility in an applied field of 100 Oe. At low field, there is no bifurcation in ZFC/FC susceptibility down to 1.8 K, indicating that there is no spin glass state or structural disorder in $\text{Ba}_6\text{Y}_2\text{Rh}_2\text{Ti}_2\text{O}_{17}$. This confirms that there is no mixing between Rh and Ti in the crystal structure.

The transmittance data for $\text{Ba}_6\text{Y}_2\text{Rh}_2\text{Ti}_2\text{O}_{17}$ powder were converted using the Kubelka-Munk method. Fitting to indirect band gap does not produce a reasonable, flat baseline, and thus the fit is done to the direct gap equation. The direct optical band gap is determined from this data

to be 0.17 eV by extrapolating the linear absorption region until it intersects with the baseline of the absorption as seen in **Figure 5**. The resistivity of $\text{Ba}_6\text{Y}_2\text{Rh}_2\text{Ti}_2\text{O}_{17}$ is plotted as a function of reciprocal temperature in the inset of **Figure 5**. The activation energy of 0.15 eV obtained by fitting the Arrhenius equation, which must be from or to defect states associated with the valence or conduction band, together with the optical data, show that $\text{Ba}_6\text{Y}_2\text{Rh}_2\text{Ti}_2\text{O}_{17}$ is a semiconductor.

Figure 6a shows the heat capacity of $\text{Ba}_6\text{Y}_2\text{Rh}_2\text{Ti}_2\text{O}_{17}$ from 0.35 to 14 K measured in magnetic fields of 0, 1, 2, 4, 5, 6 and 9 T. An upturn is seen below 3 K that is dramatically influenced in an applied magnetic field. A broad hump typical of the Schottky effect was observed at around 1 K under zero applied magnetic field³⁸. A similar upturn feature at the lowest temperatures, suppressed applied magnetic fields, has been observed in some QSL candidates^{16,21,39,40}. The low temperature heat capacity approximately obeys a universal scaling law, as shown in **Figure 6b**⁴¹. Similar to reported QSL candidates, the heat capacity data of $\text{Ba}_6\text{Y}_2\text{Rh}_2\text{Ti}_2\text{O}_{17}$ collapse at the critical point of around 0.35 K/T ^{39,40,42-44}. The power law fitting of heat capacity data in $\text{Ba}_6\text{Y}_2\text{Rh}_2\text{Ti}_2\text{O}_{17}$ results in the power of 0.57 (**Figure 6c**). This is in contrast to what is seen in conventional magnetic insulators, whose heat capacity is proportional to T^3 . We can rule out the possibility that the nuclear spins of the constituent atoms are the origin of the low temperature heat capacity behavior because the heat capacity of $\text{Ba}_6\text{Y}_2\text{Ti}_4\text{O}_{17}$ obeys the T^3 -behavior below 7 K and does not show the upturn and (**Figure 6d**). Moreover, the heat capacity values at low temperatures of TiO_2 , Y_2O_3 , BaO and RhO_2 are many orders of magnitude smaller than that of $\text{Ba}_6\text{Y}_2\text{Rh}_2\text{Ti}_2\text{O}_{17}$ ⁴⁵⁻⁴⁸.

On subtraction of the phonon contribution, the measured heat capacity data under zero applied magnetic field can be used to calculate the magnetic entropy in $\text{Ba}_6\text{Y}_2\text{Rh}_2\text{Ti}_2\text{O}_{17}$, as shown in **Figure 7**. The heat capacity of $\text{Ba}_6\text{Y}_2\text{Ti}_4\text{O}_{17}$ up to 12 K (where the heat capacity data for both

$\text{Ba}_6\text{Y}_2\text{Rh}_2\text{Ti}_2\text{O}_{17}$ and $\text{Ba}_6\text{Y}_2\text{Ti}_4\text{O}_{17}$ intersect) accounts for the phonon contribution. Surprisingly, the magnetic entropy only reaches $0.32 R \ln 2$ by 12 K. This indicates that a tremendous amount of magnetic entropy is present at lower temperatures in this material. In the inset of **Figure 7**, C/T as function of T^2 at zero applied magnetic field results in a Sommerfeld constant of $166 \text{ mJ/mol f.u. K}^2$ (or 83 mJ/mol Rh-K^2). This large value implies that heavy mass quasiparticles are present in this material. Compared to the heavy fermion superconductor Sr_2RuO_4 ($\gamma = 39 \text{ mJ/mol Ru-K}^2$)⁴⁹ or the $\text{Sr}_4\text{Rh}_3\text{O}_{10}$ layer perovskite ($\gamma = 16 \text{ mJ/mol Rh-K}^2$)²⁷ or $\text{Sr}_5\text{Rh}_4\text{O}_{12}$ ($\gamma = 30 \text{ mJ/mol-K}^2$)³⁶, $\text{Ba}_6\text{Y}_2\text{Rh}_2\text{Ti}_2\text{O}_{17}$, which is an electrical insulator, has a much larger Sommerfeld constant. This could be an interesting result for physicists and theorists to investigate.

CONCLUSIONS

$\text{Ba}_6\text{Y}_2\text{Rh}_2\text{Ti}_2\text{O}_{17}$, synthesized by a solid state method in air at ambient pressure crystallizes in a hexagonal perovskite unit cell in the $P6_3/mmc$ space group. The material has a small effective moment, $0.76 \mu_B/\text{mol-Rh}$, or $1.5 \mu_B/\text{dimer}$, compared to $1.73 \mu_B/\text{mol-Rh}$ expected for a purely ionic Rh^{4+} (spin $1/2$) system. The small negative Curie-Weiss temperature may be due to a competition between antiferromagnetic and ferromagnetic interactions, but it may alternatively indicate the dominance of very weak antiferromagnetic interactions in the material. The magnetic susceptibility and heat capacity measurements indicate that magnetic ordering is absent down to 0.35 K. The large Sommerfeld constant observed may come from the presence of a high density of low energy states, which may be due to the presence of strong magnetic fluctuations at very low temperature. The heat capacity shows an upturn under zero field at the lowest temperatures measured that is suppressed by applied fields larger than 2 T, a significant characteristic of QSL candidates. The approximate data collapse in scaled heat capacity curves further suggests that $\text{Ba}_6\text{Y}_2\text{Rh}_2\text{Ti}_2\text{O}_{17}$ may host a spin liquid ground state. Thus growing crystals of this material will

be of interest for thermal conductivity and inelastic magnetic neutron scattering experiments, as well as μ SR studies. Furthermore, the possible presence of oxygen vacancies, which will significantly impact the number of electrons on the dimers, and thus the magnetism, will be investigated by powder neutron diffraction, and the results will be reported elsewhere.

ACKNOWLEDGMENTS

The authors acknowledge the use of Princeton's Imaging and Analysis Center, which is partially supported by the Princeton Center for Complex Materials, a National Science Foundation (NSF)-MRSEC program (DMR-1420541). All of the research reported here was supported by the Institute of Quantum Matter, an Energy Frontier Research Center funded by the U.S. Department of Energy, Office of Science, Basic Energy Sciences under Award No. DE-SC0019331.

REFERENCES

- (1) Takada, K.; Sakurai, H.; Takayama-muromachi, E. Superconductivity in Two- Dimensional CoO₂ Layers. **2003**, 422 (March), 53–55 DOI: 10.1038/nature01442.1.
- (2) Singh, D. J.; Wilson-Short, G. B.; Kasinathan, D.; Suewattana, M.; Fornari, M. Electronic Structure and Disorder in Na_xCoO₂ and SrRh₂O₄. *Solid State Sci.* **2007**, 9 (7), 604–607 DOI: 10.1016/j.solidstatesciences.2007.03.008.
- (3) Zhang, B. Bin; Wang, C.; Dong, S. T.; Lv, Y. Y.; Zhang, L.; Xu, Y.; Chen, Y. B.; Zhou, J.; Yao, S. H.; Chen, Y. F. Preparation, Structure Evolution, and Metal-Insulator Transition of Na_xRhO₂ Crystals ($0.25 \leq x \leq 1$). *Inorg. Chem.* **2018**, 57 (5), 2730–2735 DOI: 10.1021/acs.inorgchem.7b03110.
- (4) Park, S.; Kang, K.; Si, W.; Yoon, W. S.; Lee, Y.; Moodenbaugh, A. R.; Lewis, L. H.; Vogt, T. Synthesis and Characterization of Na_{0.3}RhO₂·0.6H₂O - A Semiconductor with a Weak Ferromagnetic Component. *Solid State Commun.* **2005**, 135 (1–2), 51–56 DOI: 10.1016/j.ssc.2005.03.063.
- (5) Hobbie, K.; Hoppe, R. Zum Aufbau von NaRhO₂. *ZAAC - J. Inorg. Gen. Chem.* **1988**, 565 (1), 106–110 DOI: 10.1002/zaac.19885650111.
- (6) Okazaki, R.; Nishina, Y.; Yasui, Y.; Shibusaki, S.; Terasaki, I. Optical Study of the Electronic Structure and Correlation Effects in K_{0.49}RhO₂. *Phys. Rev. B - Condens. Matter Mater. Phys.* **2011**, 84 (7), 1–4 DOI: 10.1103/PhysRevB.84.075110.
- (7) Zhang, B. Bin; Lv, Y. Y.; Dong, S. T.; Zhang, L. Y.; Yao, S. H.; Chen, Y. B.; Zhang, S. T.; Zhou, J.; Chen, Y. F. Depotassiation of K_{0.62}RhO₂ and Electronic Property of the End-Product K_{0.32}RhO₂ Single Crystal. *Solid State Commun.* **2016**, 230, 1–5 DOI: 10.1016/j.ssc.2016.01.003.
- (8) Jarrett, H. S.; Sleight, A. W.; Kung, H. H.; Gillson, J. L. Photoelectrochemical Properties of LuRhO₃. *Surf. Sci.* **1980**, 101 (1–3), 205–213 DOI: 10.1016/0039-6028(80)90613-5.
- (9) Park, J. E.; Hu, Y.; Krizan, J. W.; Gibson, Q. D.; Tayvah, U. T.; Selloni, A.; Cava, R. J.; Bocarsly, A. B. Stable Hydrogen Evolution from an AgRhO₂ Photocathode under Visible Light. *Chem. Mater.* **2018**, 30 (8), 2574–2582 DOI: 10.1021/acs.chemmater.7b04911.
- (10) Lejay, P.; Etourneau, J.; Vlasse, M.; Hagenmuller, P.; Chimie, D. Structure, Superconductivity and Magnetism of New Rare Earth-Rhodium Silicides RE₂Rh₃Si₅ of U₂Co₃Si₅-Type. **1982**, 17 (c),

1211–1220.

- (11) Kuentzler, R.; Waterstrat, R. M. Electronic Properties, Superconductivity and Stability of the ZrRh Alloys. *Solid State Commun.* **1985**, *54* (6), 517–524 DOI: 10.1016/0038-1098(85)90660-X.
- (12) Carnicom, E. M.; Xie, W.; Klimczuk, T.; Lin, J.; Górnicka, K.; Sobczak, Z.; Ong, N. P.; Cava, R. J. TaRh₂B₂ and NbRh₂B₂: Superconductors with a Chiral Noncentrosymmetric Crystal Structure. *Sci. Adv.* **2018**, *4* (5) DOI: 10.1126/sciadv.aar7969.
- (13) Man, H.; Halim, M.; Sawa, H.; Hagiwara, M.; Wakabayashi, Y.; Nakatsuji, S. Spin-Orbital Entangled Liquid State in the Copper Oxide Ba₃CuSb₂O₉. *J. Phys. Condens. Matter* **2018**, *30* (44), 443002 DOI: 10.1088/1361-648X/aae106.
- (14) Sandilands, L. J.; Tian, Y.; Plumb, K. W.; Kim, Y. J.; Burch, K. S. Scattering Continuum and Possible Fractionalized Excitations in α -RuCl₃. *Phys. Rev. Lett.* **2015**, *114* (14), 1–5 DOI: 10.1103/PhysRevLett.114.147201.
- (15) Nguyen, L. T.; Halloran, T.; Xie, W.; Kong, T.; Broholm, C. L.; Cava, R. J. Geometrically Frustrated Trimer-Based Mott Insulator. *Phys. Rev. Mater.* **2018**, *2* (5), 054414 DOI: 10.1103/PhysRevMaterials.2.054414.
- (16) Nguyen, L. T.; Cava, R. J. Trimer-Based Spin Liquid Candidate Ba₄NbIr₃O₁₂. *Phys. Rev. Mater.* **2019**, *3* (1), 014412 DOI: 10.1103/PhysRevMaterials.3.014412.
- (17) Shaginyan, V. R.; Msezane, A. Z.; Popov, K. G. Thermodynamic Properties of the Kagome Lattice in Herbertsmithite. *Phys. Rev. B - Condens. Matter Mater. Phys.* **2011**, *84* (6), 1–4 DOI: 10.1103/PhysRevB.84.060401.
- (18) Abramchuk, M.; Ozsoy-Keskinbora, C.; Krizan, J. W.; Metz, K. R.; Bell, D. C.; Tafti, F. Cu₂IrO₃: A New Magnetically Frustrated Honeycomb Iridate. *J. Am. Chem. Soc.* **2017**, *139* (43), 15371–15376 DOI: 10.1021/jacs.7b06911.
- (19) Helton, J. S.; Matan, K.; Shores, M. P.; Nytko, E. A.; Bartlett, B. M.; Qiu, Y.; Nocera, D. G.; Lee, Y. S. Dynamic Scaling in the Susceptibility of the Spin-1/2 Kagome Lattice Antiferromagnet Herbertsmithite. *Phys. Rev. Lett.* **2010**, *104* (14), 1–4 DOI: 10.1103/PhysRevLett.104.147201.
- (20) Zheng, J.; Ran, K.; Li, T.; Wang, J.; Wang, P.; Liu, B.; Liu, Z. X.; Normand, B.; Wen, J.; Yu, W. Gapless Spin Excitations in the Field-Induced Quantum Spin Liquid Phase of α -RuCl₃. *Phys. Rev. Lett.* **2017**, *119* (22), 1–6 DOI: 10.1103/PhysRevLett.119.227208.

- (21) Zhong, R.; Guo, S.; Xu, G.; Xu, Z.; Cava, R. J. Strong Quantum Fluctuations in a Quantum Spin Liquid Candidate with a Co-Based Triangular Lattice. *Proc. Natl. Acad. Sci. U. S. A.* **2019**, *116* (29), 14505–14510 DOI: 10.1073/pnas.1906483116.
- (22) Banerjee, A.; Yan, J.; Knolle, J.; Bridges, C. A.; Stone, M. B.; Lumsden, M. D.; Mandrus, D. G.; Tennant, D. A.; Moessner, R.; Nagler, S. E. Neutron Scattering in the Proximate Quantum Spin Liquid α -RuCl₃. *Science* (80-.). **2017**, *356* (6342), 1055–1059 DOI: 10.1126/science.aah6015.
- (23) Balents, L. Spin Liquids in Frustrated Magnets. *Nature* **2010**, *464* (7286), 199–208 DOI: 10.1038/nature08917.
- (24) Cao, G.; Zheng, H.; Zhao, H.; Ni, Y.; Pocs, C. A.; Zhang, Y.; Ye, F.; Hoffmann, C.; Wang, X.; Lee, M.; Hermele, M.; Kimchi, I. Quantum Liquid from Strange Frustration in the Trimer Magnet Ba₄Ir₃O₁₀. **2019**.
- (25) Kuang, X.; Jing, X.; Loong, C. K.; Lachowski, E. E.; Skakle, J. M. S.; West, A. R. A New Hexagonal 12-Layer Perovskite-Related Structure: Ba₆R₂Ti₄O₁₇ (R = Nd and Y). *Chem. Mater.* **2002**, *14* (10), 4359–4363 DOI: 10.1021/cm020374m.
- (26) Vente, J. F.; Lear, J. K.; Battle, P. D. Sr_{4-*x*}Ca_{*x*}RhO₆: A Magnetically Ordered Rh IV Compound. *J. Mater. Chem.* **1995**, *5* (11), 1785–1789 DOI: 10.1039/JM9950501785.
- (27) Yamaura, K.; Huang, Q.; Young, D. P.; Takayama-Muromachit, E. Crystal Structure and Magnetic Properties of the Trilayered Perovskite Sr₄Rh₃O₁₀: A New Member of the Strontium Rhodate Family. *Chem. Mater.* **2004**, *16* (18), 3424–3430 DOI: 10.1021/cm0491072.
- (28) Amusia, M. Y.; Popov, K. G.; Shaginyan, V. R.; Stephanovich, V. A. *Theory of Heavy-Fermion Compounds*; 2015; Vol. 182.
- (29) Toby, B. H. EXPGUI, a Graphical User Interface for GSAS. *J. Appl. Crystallogr.* **2001**, *34* (2), 210–213 DOI: 10.1107/S0021889801002242.
- (30) Momma, K.; Izumi, F. VESTA 3 for Three-Dimensional Visualization of Crystal, Volumetric and Morphology Data. *J. Appl. Crystallogr.* **2011**, *44* (6), 1272–1276 DOI: 10.1107/S0021889811038970.
- (31) Stitzer, K. E.; El Abed, A.; Darriet, J.; Zur Loye, H. C. Crystal Growth and Structure Determination of Barium Rhodates: Stepping Stones toward 2H-BaRhO₃. *J. Am. Chem. Soc.* **2004**, *126* (3), 856–864 DOI: 10.1021/ja0374271.

- (32) Xu, L.; Yadav, R.; Yushankhai, V.; Siurakshina, L.; Van Den Brink, J.; Hozoi, L. Superexchange Interactions between Spin-Orbit-Coupled $J \approx 1/2$ Ions in Oxides with Face-Sharing Ligand Octahedra. *Phys. Rev. B* **2019**, *99* (11) DOI: 10.1103/PhysRevB.99.115119.
- (33) Yamaura, K.; Takayama-Muromachi, E. High-Pressure Synthesis of the Perovskite Rhodate CaRhO_3 . *Phys. C Supercond. its Appl.* **2006**, *445–448* (1–2), 54–56 DOI: 10.1016/j.physc.2006.03.076.
- (34) Yamaura, K.; Huang, Q.; Moldovan, M.; Young, D. P.; Sato, A.; Baba, Y.; Nagai, T.; Matsui, Y.; Takayama-Muromachi, E. High-Pressure Synthesis, Crystal Structure Determination, and a Ca Substitution Study of the Metallic Rhodium Oxide NaRh_2O_4 . *Chem. Mater.* **2005**, *17* (2), 359–365 DOI: 10.1021/cm0483846.
- (35) Yamaura, K.; Young, D. P.; Takayama-Muromachi, E. Magnetic Studies of the Lightly Ru Doped Perovskite Rhodates $\text{Sr}(\text{Ru,Rh})\text{O}_3$. *Phys. B Condens. Matter* **2005**, *359–361* (SPEC. ISS.), 1261–1263 DOI: 10.1016/j.physb.2005.01.394.
- (36) Cao, G.; Durairaj, V.; Chikara, S.; Parkin, S.; Schlottmann, P. Partial Antiferromagnetism in Spin-Chain $\text{Sr}_5\text{Rh}_4\text{O}_{12}$, $\text{Ca}_5\text{Ir}_3\text{O}_{12}$, and Ca_4IrO_6 Single Crystals. *Phys. Rev. B - Condens. Matter Mater. Phys.* **2007**, *75* (13), 1–9 DOI: 10.1103/PhysRevB.75.134402.
- (37) Stitzer, K. E.; Smith, M. D.; Darriet, J.; Loye, H. C. zu. Crystal Growth, Structure Determination and Magnetism of a New Hexagonal Rhodate: $\text{Ba}_9\text{Rh}_8\text{O}_{24}$. *Chem. Commun.* **2001**, *17*, 1680–1681 DOI: 10.1039/b104513j.
- (38) Gopal, E. S. R. *Specific Heat at Low Temperatures*; 1996.
- (39) Sheckelton, J. P.; Neilson, J. R.; Soltan, D. G.; McQueen, T. M. Possible Valence-Bond Condensation in the Frustrated Cluster Magnet $\text{LiZn}_2\text{Mo}_3\text{O}_8$. *Nat. Mater.* **2012**, *11* (6), 493–496 DOI: 10.1038/nmat3329.
- (40) Kitagawa, K.; Takayama, T.; Matsumoto, Y.; Kato, A.; Takano, R.; Kishimoto, Y.; Bette, S.; Dinnebier, R.; Jackeli, G.; Takagi, H. A Spin-Orbital-Entangled Quantum Liquid on a Honeycomb Lattice. *Nature* **2018**, *554* (7692), 341–345 DOI: 10.1038/nature25482.
- (41) Kimchi, I.; Sheckelton, J. P.; McQueen, T. M.; Lee, P. A. Scaling and Data Collapse from Local Moments in Frustrated Disordered Quantum Spin Systems. *Nat. Commun.* **2018**, *9* (1), 1–5 DOI: 10.1038/s41467-018-06800-2.
- (42) Sheckelton, J. P.; Foronda, F. R.; Pan, L.; Moir, C.; McDonald, R. D.; Lancaster, T.; Baker, P. J.;

- Armitage, N. P.; Imai, T.; Blundell, S. J.; McQueen, T. M. Local Magnetism and Spin Correlations in the Geometrically Frustrated Cluster Magnet $\text{LiZn}_2\text{Mo}_3\text{O}_8$. *Phys. Rev. B - Condens. Matter Mater. Phys.* **2014**, *89* (6), 1–7 DOI: 10.1103/PhysRevB.89.064407.
- (43) Mourigal, M.; Fuhrman, W. T.; Sheckelton, J. P.; Wartelle, A.; Rodriguez-Rivera, J. A.; Abernathy, D. L.; McQueen, T. M.; Broholm, C. L. Molecular Quantum Magnetism in $\text{LiZn}_2\text{Mo}_3\text{O}_8$. *Phys. Rev. Lett.* **2014**, *112* (2), 1–5 DOI: 10.1103/PhysRevLett.112.027202.
- (44) Helton, J. S.; Matan, K.; Shores, M. P.; Nytko, E. A.; Bartlett, B. M.; Yoshida, Y.; Takano, Y.; Suslov, A.; Qiu, Y.; Chung, J. H.; Nocera, D. G.; Lee, Y. S. Spin Dynamics of the Spin-1/2 Kagome Lattice Antiferromagnet $\text{ZnCu}_3(\text{OH})_6\text{Cl}_2$. *Phys. Rev. Lett.* **2007**, *98* (10), 4–7 DOI: 10.1103/PhysRevLett.98.107204.
- (45) Jacob, K. T.; Prusty, D. Thermodynamic Properties of RhO_2 . *Journal of Alloys and Compounds*. Elsevier Ltd September 24, 2010, pp L17–L20.
- (46) Mgo, B.-; Cao, B.-; Al, B.-; Sio, B.-. *A Thermodynamic Assessment of the BaO-MgO, BaO-CaO, BaO-Al₂O₃ and BaO-SiO₂ Systems*; 2014.
- (47) Yang, F.; Zhao, X.; Xiao, P. Thermal Conductivities of YSZ/ Al_2O_3 Composites. *J. Eur. Ceram. Soc.* **2010**, *30* (15), 3111–3116 DOI: 10.1016/j.jeurceramsoc.2010.07.007.
- (48) Schliesser, J. M.; Smith, S. J.; Li, G.; Li, L.; Walker, T. F.; Parry, T.; Boerio-Goates, J.; Woodfield, B. F. Heat Capacity and Thermodynamic Functions of Nano- TiO_2 Rutile in Relation to Bulk- TiO_2 Rutile. *J. Chem. Thermodyn.* **2015**, *81*, 311–322 DOI: 10.1016/j.jct.2014.08.002.
- (49) Maeno, Y. Evidence for Spin-Triplet Superconductivity in Sr_2RuO_4 . *Phys. B Condens. Matter* **2000**, *281–282*, 865–871 DOI: 10.1016/S0921-4526(99)00849-2.

Table 1. Structural parameters for Ba₆Y₂Rh₂Ti₂O₁₇ at 300 K. Space group *P6₃/mmc* (No. 194).

Atom	Wyckoff.	Occ.	<i>x</i>	<i>y</i>	<i>z</i>	<i>U_{iso}</i>
Ba1	4f	1	1/3	2/3	0.18094(6)	0.0091(6)
Ba2	4f	1	1/3	2/3	0.58950(6)	0.0124(6)
Ba3	2a	1	0	0	0	0.0435(14)
Ba4	2b	1	0	0	1/4	0.0119(10)
Rh	4f	1	1/3	2/3	0.70592(10)	0.0455(10)
Ti	4f	1	1/3	2/3	0.05146(24)	0.0218(20)
Y	4e	1	0	0	0.12544(10)	0.0067(10)
O1	12k	1	0.1930(10)	0.3861(19)	0.42554(31)	0.0311(20)
O2	12k	1	0.1629(10)	0.3258(21)	0.83969(31)	0.0311(20)
O3	6h	1	0.4982(11)	-0.0035(22)	1/4	0.0311(20)
O4	4f	1	1/3	2/3	0.5072(6)	0.0311(20)

$a = b = 5.920426(20)$ Å, $c = 29.49740(18)$ Å, $V = 895.407(5)$ Å³, $\alpha = \beta = 90^\circ$, $\gamma = 120^\circ$.

$\chi^2 = 3.71$, $R_{wp} = 11.18\%$, $R_p = 7.91\%$, $R_F^2 = 8.91\%$

Table 2: Selected interatomic distances (Å) for Ba₆Y₂Rh₂Ti₂O₁₇ at 300 K.

	Interatomic distance (Å)
Rh-O2 (x3)	2.206(11)
Rh-O3 (x3)	2.162(10)
Ba1-O2 (x6)	3.022(9)
Ba1-O3 (x3)	2.648(8)
Ba2-O1 (x6)	3.006(9)
Ba2-O2 (x3)	2.723(10)
Ba2-O4 (x1)	2.428(18)
Ba3-O1 (x6)	2.957(10)
Ba4-O2 (x6)	3.129(10)
Ba4-O3 (x6)	2.960(10)
Ti-O1 (x3)	1.590(11)
Ti-O4 (x1)	1.73(2)
Y-O1 (x3)	2.486(10)
Y-O2 (x3)	1.962(11)

Figure Captions:

Figure 1: (a) Rietveld powder x-ray diffraction refinement of the crystal structure of $\text{Ba}_6\text{Y}_2\text{Rh}_2\text{Ti}_2\text{O}_{17}$ in the space group $P6_3/mmc$ (No. 194). $\chi^2 = 3.65$, $R_{\text{wp}} = 11.1\%$, $R_p = 7.74\%$, $R_F^2 = 8.72\%$. The observed x-ray pattern is shown in black, calculated in red, difference in blue, and tick marks denoting allowed peak positions in pink. The inset shows the details of the data and fit at higher angles. Also the SEM/EDS analysis of $\text{Ba}_6\text{Y}_2\text{Rh}_2\text{Ti}_2\text{O}_{17}$ confirms the elemental ratios. (b) The TGA analysis of $\text{Ba}_6\text{Y}_2\text{Rh}_2\text{Ti}_2\text{O}_{17-\delta}$ suggests the possible presence of oxygen vacancies.

Figure 2: (a) Crystal structure of $\text{Ba}_6\text{Y}_2\text{Rh}_2\text{Ti}_2\text{O}_{17}$. (b) Triangular lattice of Rh^{4+} magnetic ions in the ab plane. (c) Rh_2O_9 dimer (two face-sharing RhO_6 octahedra). There are different Rh-O bond lengths, 2.16 Å and 2.21 Å. The Rh-Rh distance within the dimer is 2.60 Å.

Figure 3: Temperature dependent magnetic susceptibility of $\text{Ba}_6\text{Y}_2\text{Rh}_2\text{Ti}_2\text{O}_{17}$ under 2 kOe applied magnetic field. The curves for the higher fields start to deviate below 10 K, consistent with the magnetization data in the inset.

Figure 4: Temperature dependent magnetic susceptibility in $\text{Ba}_6\text{Y}_2\text{Rh}_2\text{Ti}_2\text{O}_{17}$ at the applied field of 2 kOe. Inset: Curie-Weiss fitting from 10-50 K results in the effective moment of $0.76 \mu_B/\text{mol-Rh}$ and the Curie-Weiss constant of -2.8 K. ZFC/FC magnetic susceptibility of $\text{Ba}_6\text{Y}_2\text{Rh}_2\text{Ti}_2\text{O}_{17}$ under a small applied magnetic field of 100 Oe. The absence of bifurcation between ZFC (black squares) and FC (red circles) rules out the possibility of spin glass behavior and atomic disorder in this material.

Figure 5: An FTIR with an ATR sample accessory was employed to estimate the optical bandgap (0.17 eV) for a direct transition by extrapolating the linear absorption region through the black lines until it intersects with the baseline of the absorption. (For indirect band gap, it does not have a flat absorption baseline). Inset: Resistivity measurement on $\text{Ba}_6\text{Y}_2\text{Rh}_2\text{Ti}_2\text{O}_{17}$ resulting in a transport gap of 0.15 eV.

Figure 6: (a) Heat capacity divided by temperature for $\text{Ba}_6\text{Y}_2\text{Rh}_2\text{Ti}_2\text{O}_{17}$ measured under different applied magnetic fields below 15 K. At zero field, the presence of a high density of low energy states is evidenced by the presence of a large upturn that persists down to the lowest temperature of the measurement. (b) The universal scaling of heat capacity data collapsed at the critical point⁴¹.

(c) The power law fitting of the raw heat capacity data in $\text{Ba}_6\text{Y}_2\text{Rh}_2\text{Ti}_2\text{O}_{17}$ results in the power of 0.57. The small hump at 1 K may come from the Schottky effect, where the spins are populated from one to another energy level. Inset: The existence of heavy quasiparticles in insulating $\text{Ba}_6\text{Y}_2\text{Rh}_2\text{Ti}_2\text{O}_{17}$ is supported by a very large Sommerfeld constant [$\gamma = 166 \text{ mJ mol}_{\text{f.u.}}^{-1} \text{ K}^{-2}$]. (d) We rule out the possibility that the observed behavior arises from the nuclear spins of the constituent atoms by measuring the heat capacity of $\text{Ba}_6\text{Y}_2\text{Ti}_4\text{O}_{17}$ (no upturn observed). Moreover, the nuclear spins in TiO_2 , Y_2O_3 , BaO and RhO_2 result in a low temperature heat capacity many orders of magnitude smaller than the value of 700 mJ/mol-K^2 at 0.35 K seen in $\text{Ba}_6\text{Y}_2\text{Rh}_2\text{Ti}_2\text{O}_{17}$.

Figure 7: C/T vs. T in $\text{Ba}_6\text{Y}_2\text{Rh}_2\text{Ti}_2\text{O}_{17}$ measured down to 0.35 K under zero applied magnetic field. Below 1 K, the upturn indicates the presence of spin fluctuations. The heat capacity of $\text{Ba}_6\text{Y}_2\text{Ti}_4\text{O}_{17}$ below 12 K was used to model the phonon contribution. The magnetic entropy is calculated to be $1.86 \text{ J/mol}^{-1}\text{K}^{-1}$, accounting for about 1/3 of the magnetic entropy of an Ising or a spin $1/2$ Heisenberg system.

Figures:

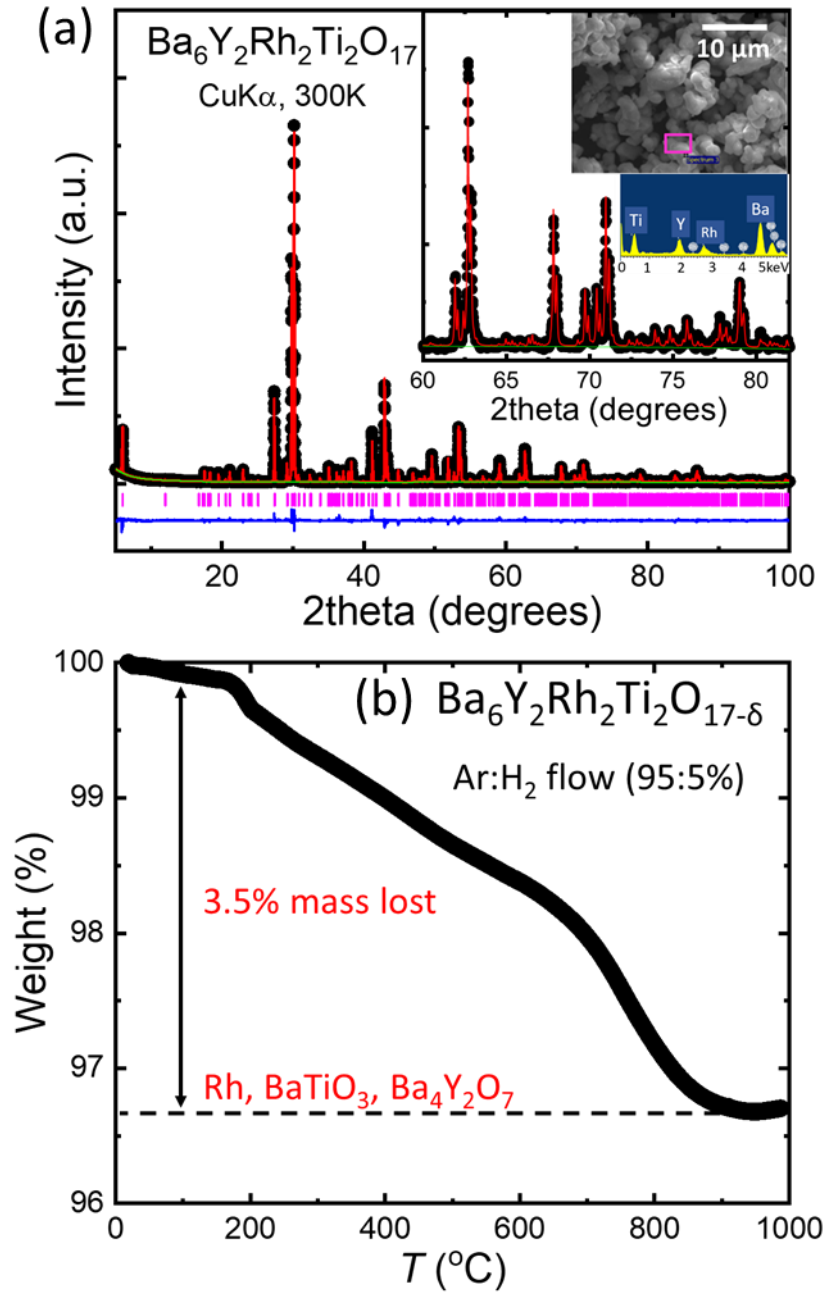


Figure 1.

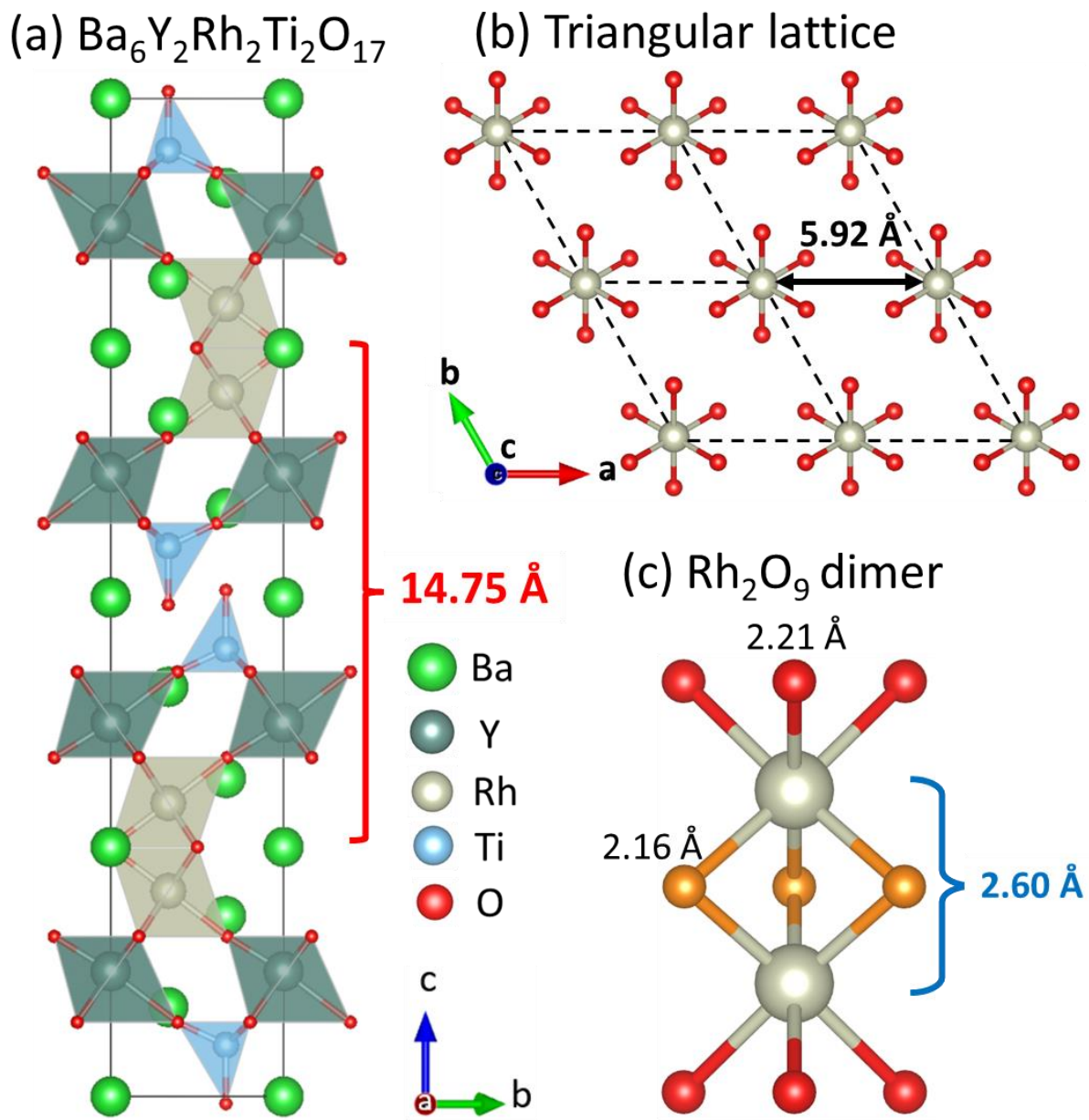


Figure 2.

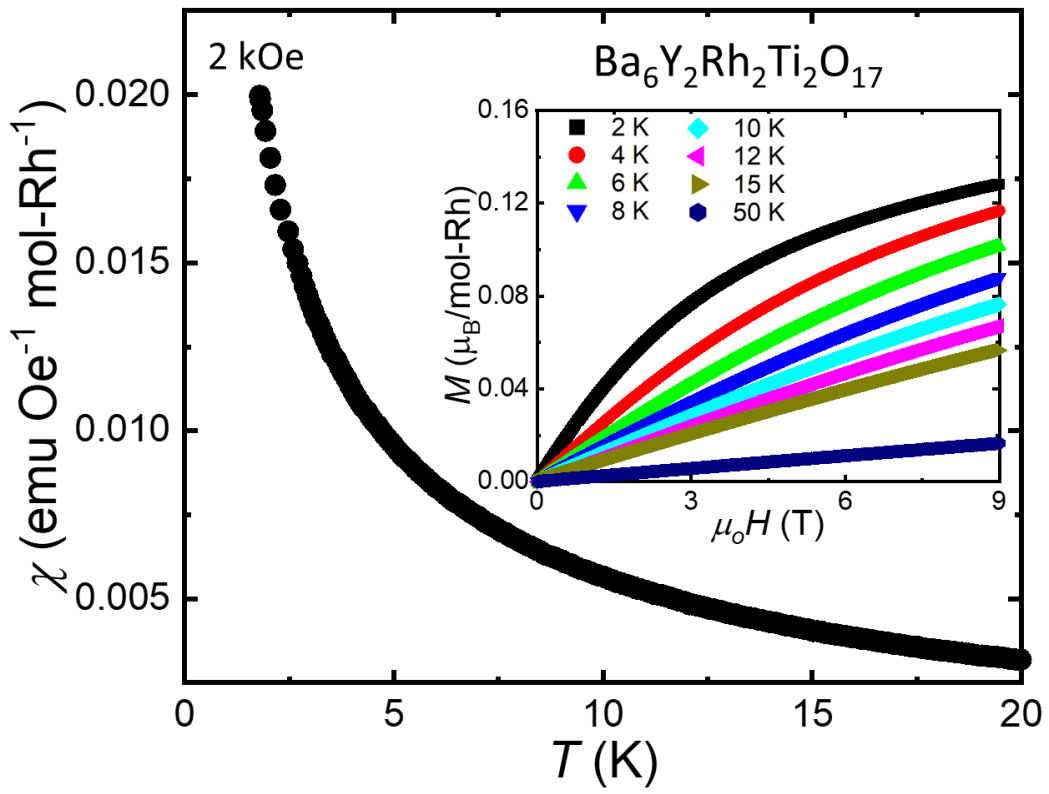


Figure 3.

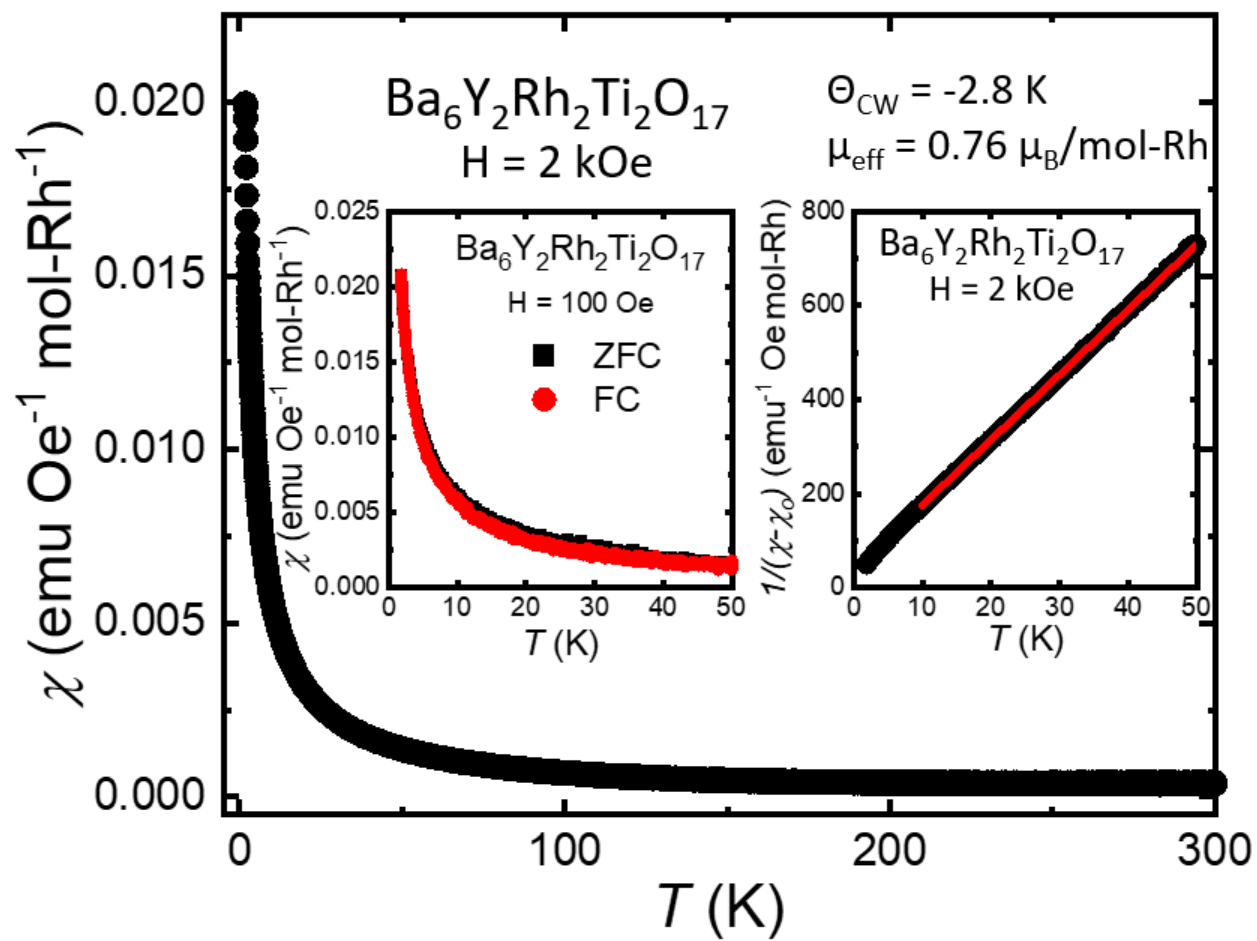


Figure 4.

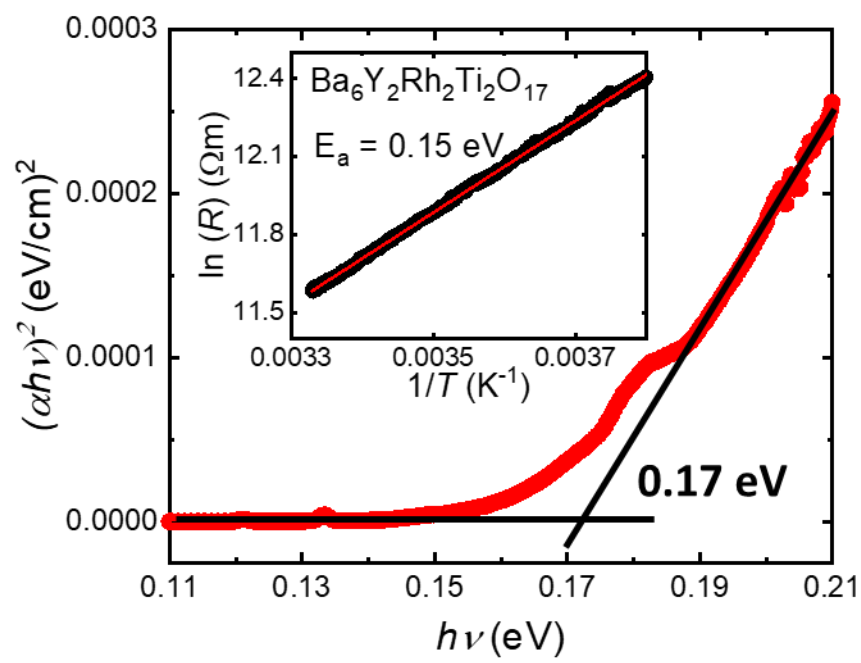


Figure 5.

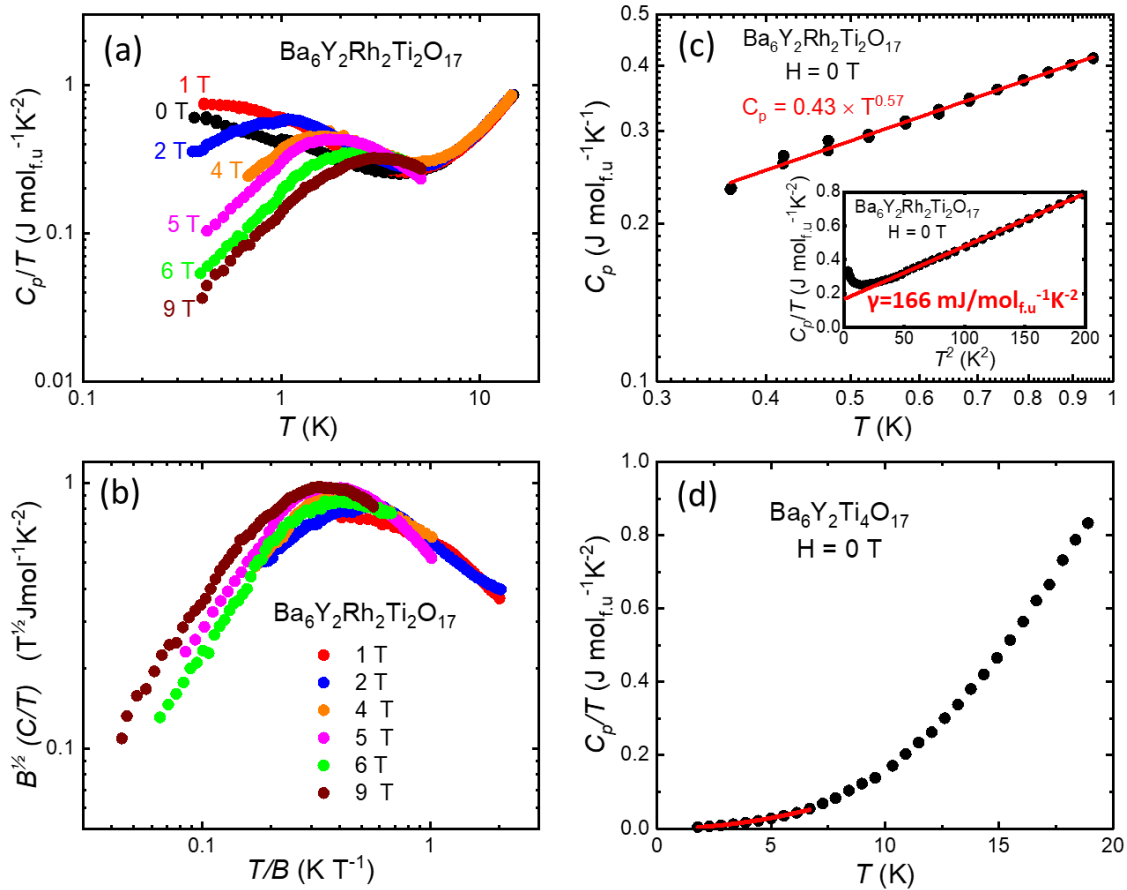


Figure 6.

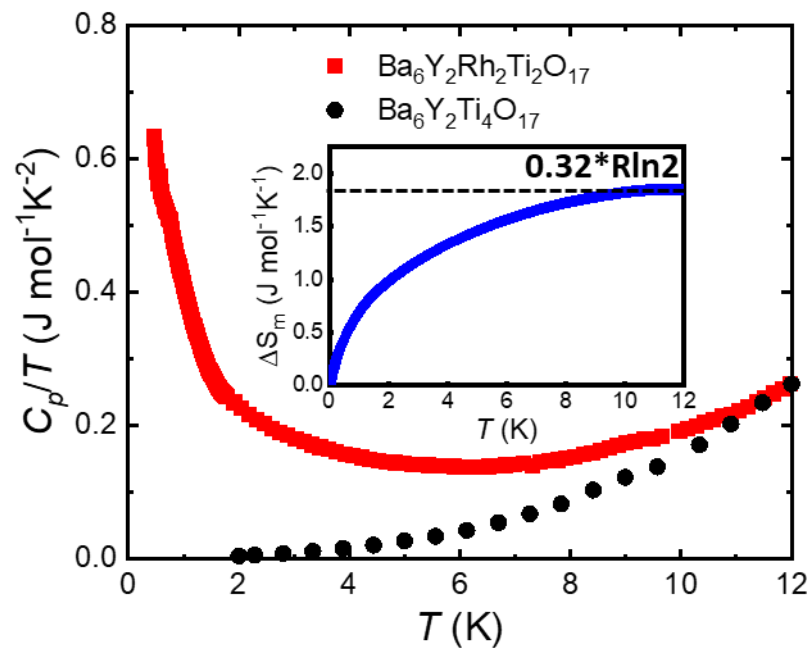


Figure 7.